



Article

Beijing Land Subsidence Revealed Using PS-InSAR with Long Time Series TerraSAR-X SAR Data

Zechao Bai ^{1,2} , Yanping Wang ^{2,*} and Timo Balz ³

¹ School of Electrical and Control Engineering, North China University of Technology, Beijing 100144, China; baizechao1991@163.com

² Radar Monitoring Technology Laboratory, School of Information Science and Technology, North China University of Technology, Beijing 100144, China

³ State Key Laboratory of Information Engineering in Surveying, Mapping and Remote Sensing (LIESMARS), Wuhan University, Wuhan 430079, China; balz@whu.edu.cn

* Correspondence: wangyp@ncut.edu.cn

Abstract: Beijing is a major city suffering from land subsidence due to long-term over-exploitation of groundwater. The South-to-North Water Diversion Project (SNWDP), however, has had a significant impact on the structure of water consumption since the end of 2014, and it is changing the status of land subsidence in Beijing. In this study, we employed Persistent Scatterers Synthetic Aperture Radar Interferometric (PS-InSAR) to investigate the decadal evolution of land subsidence in Beijing with 100 TerraSAR-X stripmap images collected from April 2010 to December 2019. The water resources, historic climate and urban construction data were compiled for the years of 2010 to 2019 to analyze changes in groundwater level, human activity, surface geology, active faults and land subsidence patterns. The results show that the changes in the water supply structure are correlated to a rise in groundwater level after 2015. These changes include an increase in the water supply from the SNWDP, a reduction in groundwater exploitation, the optimization of water consumption, replacing recycled water for environmental water and a reduction in the use of water for agriculture. Land subsidence in the study area was concentrated in the eastern regions, trending towards a decreasing velocity starting about two years after the commencement of SNWDP in 2015. Uneven subsidence in the land subsidence area was related to excavations of underground soil, and the construction of Line 6 and Line 7 led to rapid nonlinear subsidence. Our results have scientific significance for reducing subsidence hazards in the context of SNWDP and urban expansion.

Keywords: Beijing; land subsidence; PS-InSAR; South-to-North Water Diversion Project; subway network



Citation: Bai, Z.; Wang, Y.; Balz, T. Beijing Land Subsidence Revealed Using PS-InSAR with Long Time Series TerraSAR-X SAR Data. *Remote Sens.* **2022**, *14*, 2529. <https://doi.org/10.3390/rs14112529>

Academic Editor: Michele Saroli

Received: 22 April 2022

Accepted: 23 May 2022

Published: 25 May 2022

Publisher's Note: MDPI stays neutral with regard to jurisdictional claims in published maps and institutional affiliations.



Copyright: © 2022 by the authors. Licensee MDPI, Basel, Switzerland. This article is an open access article distributed under the terms and conditions of the Creative Commons Attribution (CC BY) license (<https://creativecommons.org/licenses/by/4.0/>).

1. Introduction

Land subsidence is a serious geological challenge, which can be caused by over-exploiting groundwater. At least 200 areas in 34 countries have suffered land subsidence caused by the exploitation of groundwater in the past century [1]. These countries include but are not limited to China [2], the United States [3,4], Mexico [5], Indonesia [6], Iran [7], Egypt [8], Italy [9–16], Spain [17,18] and the Netherlands [19,20]. The increasing development of land and water resources threatens to exacerbate existing land subsidence problems and initiate new problems.

Land subsidence is a major concern for city managers globally, putting infrastructure at risk of damage. In China, Beijing [21], Shanghai [22], Xi'an [23] and Wuhan [24] are suffering from land subsidence. Previous studies have shown that the land subsidence in Beijing is caused by: (1) groundwater over-exploitation and (2) urban buildings and infrastructures [2]. Over the past decade, Beijing has been a city that has depended on groundwater as the main water supply source. Groundwater resources have been over-exploited, accounting for 37~65% of the total water supply. Moreover, Beijing, by the end of 2020, had the second largest urban rail transit system in China, with 382 operating

stations and 799.1 km of operating lines, including 653 km of subway lines. Owing to the over-exploitation of groundwater and urban construction, Beijing has formed multiple land subsidence areas. However, since the end of 2014, the SNWDP has altered the water consumption structure of Beijing, changing the status of land subsidence. Thus, land subsidence changes should be comprehensively investigated and evaluated.

In order to abate and mitigate subsidence-related disasters, it is necessary to obtain a high-precision and current spatiotemporal distribution of land subsidence in Beijing. Technologies including leveling and GNSS have been used, but their low spatial resolutions and high costs limit their application for large-scale monitoring. Synthetic aperture radar interferometric (InSAR) has the advantages of high spatiotemporal resolution [25,26], low cost and large coverage [27], and it has been widely applied to land subsidence [28]. Multi-temporal InSAR, such as PS-InSAR [29], Small Baseline Subset (SBAS)-InSAR [30], Temporarily Coherent Point (TCP)-InSAR [31] and Quasi PS (QPS)-InSAR [32] are widely used to measure large-scale urban land subsidence at millimeter accuracy. With respect to InSAR data, the 3 m spatial resolution data show the fine details of urban land subsidence [33]. The InSAR technology based on high-resolution data can meet the current monitoring needs of urban land subsidence.

Several studies have detected land subsidence in Beijing using varying methods and InSAR data. Based on their work, we have a solid understanding of the spatial location and physical process of land subsidence [34–57]. Table 1 summarizes a selection of representative studies. These studies focused on natural and human factors to analyze the causes of land subsidence. Moreover, the key natural factors include groundwater [45,49,53,54], surface geology [41] and active faults [46,57]. Previous studies demonstrated that the main natural cause of land subsidence is groundwater over-exploitation, but there have been few studies on the relationship between the SNWDP, groundwater level variations and land subsidence. In addition, the key human impact factors include urban construction [48,50]. Previous studies mostly focused on the land subsidence of urban infrastructure during the operation periods. Uneven land subsidence was analyzed by using information such as the deformation rate. However, there have been few studies concerning land subsidence during urban infrastructure construction.

Table 1. Representative studies of Beijing land subsidence.

| Study | Method | Dataset | Key Results |
|-------------------------|-------------|---|--|
| Zhu et al., 2015 [37] | PS-InSAR | 37 ENVISAT ASAR (200306-201001) | The thickness of compressible sediments is related to the distribution of uneven land subsidence. |
| Zhang et al., 2016 [40] | MCTSB-InSAR | 21 ERS-1/2 (199205-200006) 24 ENVISAT ASAR (200306-201009) 19 RADARSAR-2 (201201-201407) | There are differences in spatial distribution and intensity of land subsidence within the monitoring time. |
| Zhou et al., 2018 [45] | PS-InSAR | 48 ENVISAT ASAR (200306-201008) 51 TerraSAR-X (201004-201512) 40 RADARSAR-2 (201106-201512) | The subsidence area is related to the groundwater depression area. |
| Gao et al., 2019 [46] | QPS-InSAR | 63 TerraSAR-X (201004-201712) | The uneven land subsidence distribution is affected by the faults. |
| Chen et al., 2021 [54] | PS-InSAR | 46 ENVISAT ASAR (200306-201008) 48 TerraSAR-X (201005-201511) | The thickness of compressible sediments and groundwater levels are related to the distribution of land subsidence. |
| Wang et al., 2021 [55] | PS-InSAR | 31 Sentinel-1 (201506-201703) 49 TerraSAR-X (201501-201703) | There is differential deformation in the Beijing Tianjin Intercity Railway. |

These studies investigated land subsidence in a multi-temporal dimension, although with different datasets with spatial resolution differences and temporal gaps. However, previous studies in Beijing were limited by incomplete and discontinuous observations,

which are insufficient for a comprehensive assessment of land subsidence. These analyses are limited to medium resolution data or high-resolution data collected for only a few years. There is a lack of in-depth understanding of the spatial expansion, intensity and temporal evolution of land subsidence as it developed in Beijing from 2010 to 2019. Thus, the key objectives of the current study are: (1) to conduct a comprehensive analysis with X-band high spatial resolution InSAR data and to map the spatiotemporal evolution of land subsidence from 2010 to 2019; (2) to study how groundwater level may affect land subsidence patterns both qualitatively and quantitatively at different stages in the context of the SNWDP; and (3) to analyze the effects of urban infrastructure construction at different stages on land subsidence.

2. Study Area

Beijing is located in the northern part of the North China Plain, with a total area of 16,410 km². The terrain is high in the northwest and low in the southeast, with an average elevation of 43.5 m. The study area is located in the middle of Beijing, including ten regions (Haidian, Chaoyang, Shunyi, Xicheng, Dongcheng, Fengtai, Daxing, Changping, Shijingshan and Tongzhou), as shown in Figure 1. The main active faults include the Nankou-Sunhe Fault (F1), Gaoliying Fault (F2), Shunyi Fault (F3), Huangzhuang Fault (F4) and Nanyuan-Tongxian Fault (F5). The Quaternary stratum of the Beijing Plain is vertically divided into three main aquifer groups, according to the depth of groundwater. The thickness of Quaternary alluvial sediments in the study area are mainly clay and medium-fine sand (Figure 2). The average annual precipitation is about 585 mm, which is concentrated in the summer from June to September.

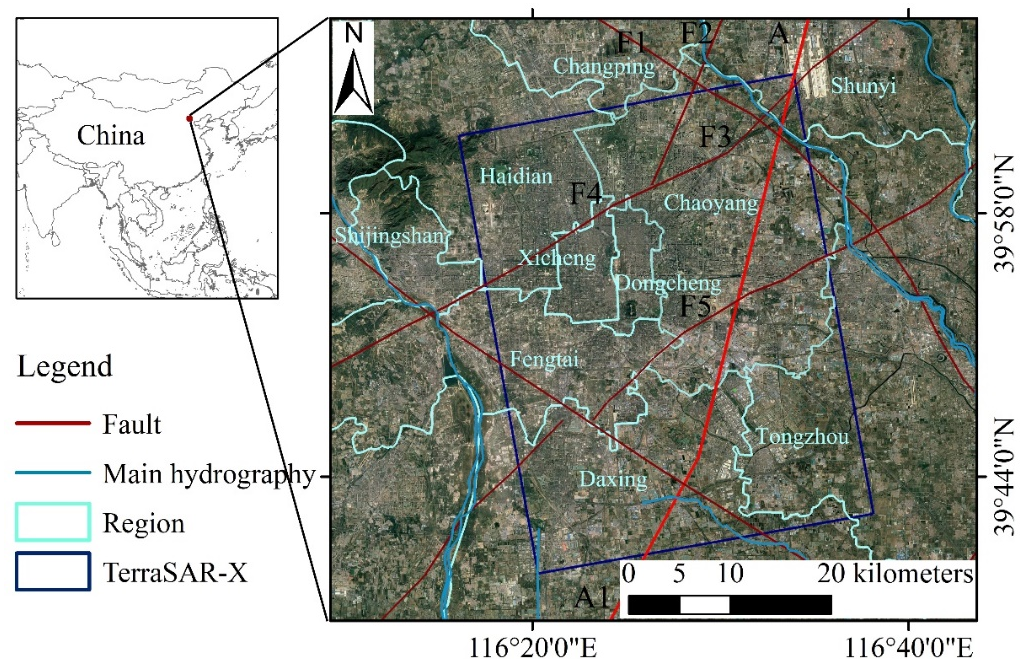


Figure 1. The study area and the coverage of InSAR data. Red lines represent major fault lines. The location of faults are derived from [49]. The hydrogeological profile used is shown in Figure 2 (A-A1). The background is a satellite image from Google Earth.

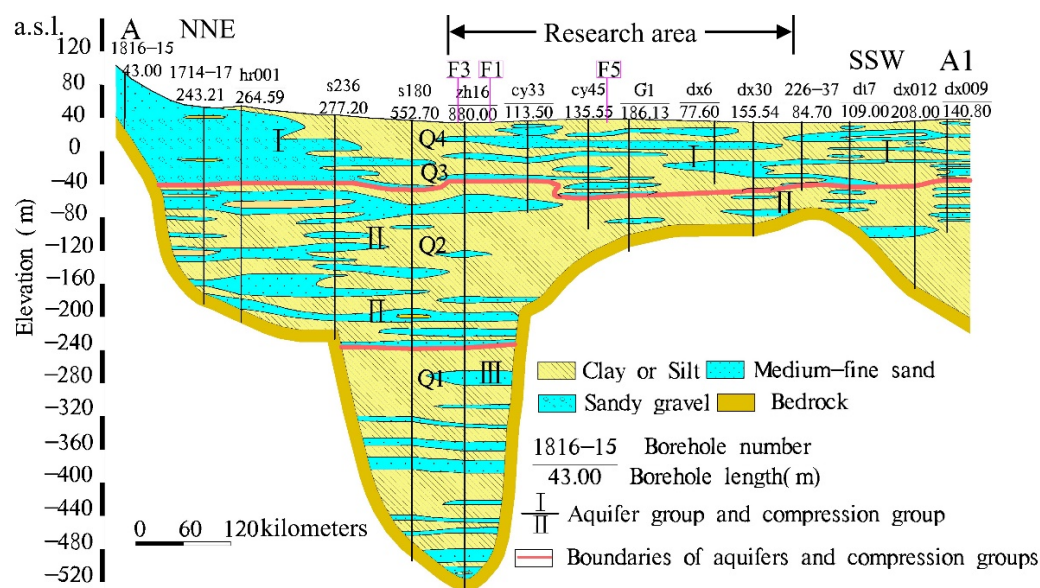


Figure 2. Hydrogeological profile (the geological data are derived from [53,57]). The aquifer system can be vertically divided into three main aquifer groups: the first compression group (Q4 + Q3), the second compression group (Q2) and the third compression group (Q1).

3. Datasets and Methodology

3.1. Datasets

The 100 X-band TerraSAR-X images from 13 April 2010 to 13 December 2019 were used. The acquisition properties of InSAR images are presented in Table 2. The Shuttle Radar Terrain Mission DEM with a spatial resolution of 90 m was used to remove the terrain phase and to geocode the InSAR results. The leveling data of two stations in Beijing from 2010 to 2013 were obtained [46]. Water resource data and precipitation data were obtained from the homepage of the public website of the Beijing Water Authority (<http://swj.beijing.gov.cn/zwgk/szygb/> (accessed on 22 April 2022)). Population data and public park area data were obtained from the homepage of the public website of the Beijing Municipal Bureau Statistics (<http://nj.tj.beijing.gov.cn/nj/main/2021-tjn/zk/indexch.htm> (accessed on 22 April 2022)). Subway data were obtained from the homepage of the public website of the China Association of Metros (<https://www.camet.org.cn/tjxx/7647> (accessed on 22 April 2022)).

Table 2. Properties of the TerraSAR-X datasets.

| Parameter | TerraSAR-X |
|------------------------|--------------------------|
| Band | X |
| Wavelength (cm) | 3.1 |
| Incident angle (°) | 33.2 |
| Product type | SLC |
| Polarization | HH |
| Sensor mode | Stripmap |
| Orbit direction | Ascending |
| Spatial resolution (m) | 3 |
| No. of images | 100 |
| Time range | April 2010–December 2019 |

According to the report of the Beijing Water Authority, groundwater exploitation was decreasing year by year after the SNWDP in Beijing at the end of 2014. According to the report of the Beijing Municipal Bureau Statistics, the resident population of Beijing was about 21.89 million in 2020, which was an increase of about 11.6% over the population of about 19.619 million in 2010. According to the 2020 report of the China Association of Metros, Beijing had the second largest urban rail transit system in China by the end of 2020, with 382 operating stations and 799.1 km of operating lines, including 653 km of subway lines. Moreover, the length of the subway line under construction was 364.7 km.

3.2. Methodology

The deformation is usually assumed to be the linear velocity in the traditional PS-InSAR, which applies to land subsidence in a limited period of time. In the 10-year observation time and with wide coverage, the targets may have nonlinear and thermal expansion deformation; therefore, the assumption of linear velocity is unreasonable. In this study, we adopted the nonlinear deformation model:

$$\Delta\phi_{diff} = \frac{4\pi}{\lambda} T\Delta v + \frac{4\pi}{\lambda} \frac{B_{\perp}}{R \sin\theta} \Delta h + \Delta\phi_{atm} + \Delta\phi_{noise} \quad (1)$$

where $\Delta\phi_{diff}$ is the differential interference phase, λ is the wavelength, T is the time baseline, B_{\perp} is the spatial baseline, R is the slant distance and θ is the incidence angle. Δv is the linear deformation, Δh is the residual height, $\Delta\phi_{atm}$ is the atmospheric phase screen and $\Delta\phi_{noise}$ is the noise. The intelligent mode in SARproZ [24,58] was used, assuming that the velocity was linearly related in time only within a small moving window (i.e., five images in our processing flow). Therefore, this approach allows for the estimation of the nonlinear deformation, which is very important for a long time series displacement and large-scale area.

The PS-InSAR method from image acquisition to InSAR results is summarized as follows (Figure 3), including conventional differential InSAR [59] and a customized two-layer network PS-InSAR. The imagery acquired on 19 October 2014 was selected as the reference image. In the step of atmospheric phase screen (APS), a small number of points with high phase stability were selected (the amplitude dispersion threshold was 0.22, and 86,411 points were selected) to estimate the accurate atmospheric phase screen, i.e., the first layer network. Then, the amplitude dispersion threshold was 0.35, increasing the number of points in the second layer network. A total of 950,789 points were selected to optimize the detection of areas around the city, such as bare ground and rocks. The two-layer network methodology was used to better improve the results and to increase the density of points. Finally, a reference point was located on a railway contact net pillar, which was assumed to be stable. The reference point coordinates were 39.870687°N, 116.420877°E. The absolute time series displacement and absolute deformation rate were generated to characterize the land subsidence.

Furthermore, we obtained four leveling measurement values of two benchmarks to evaluate the accuracy of the InSAR results. Firstly, the nearest point of each benchmark was used as the value of the InSAR result. Then, the Line of Sight (LOS) value of the InSAR result was projected onto the vertical direction according to the incident angle of the images. Finally, one benchmark was used as a reference to correct the other benchmark.

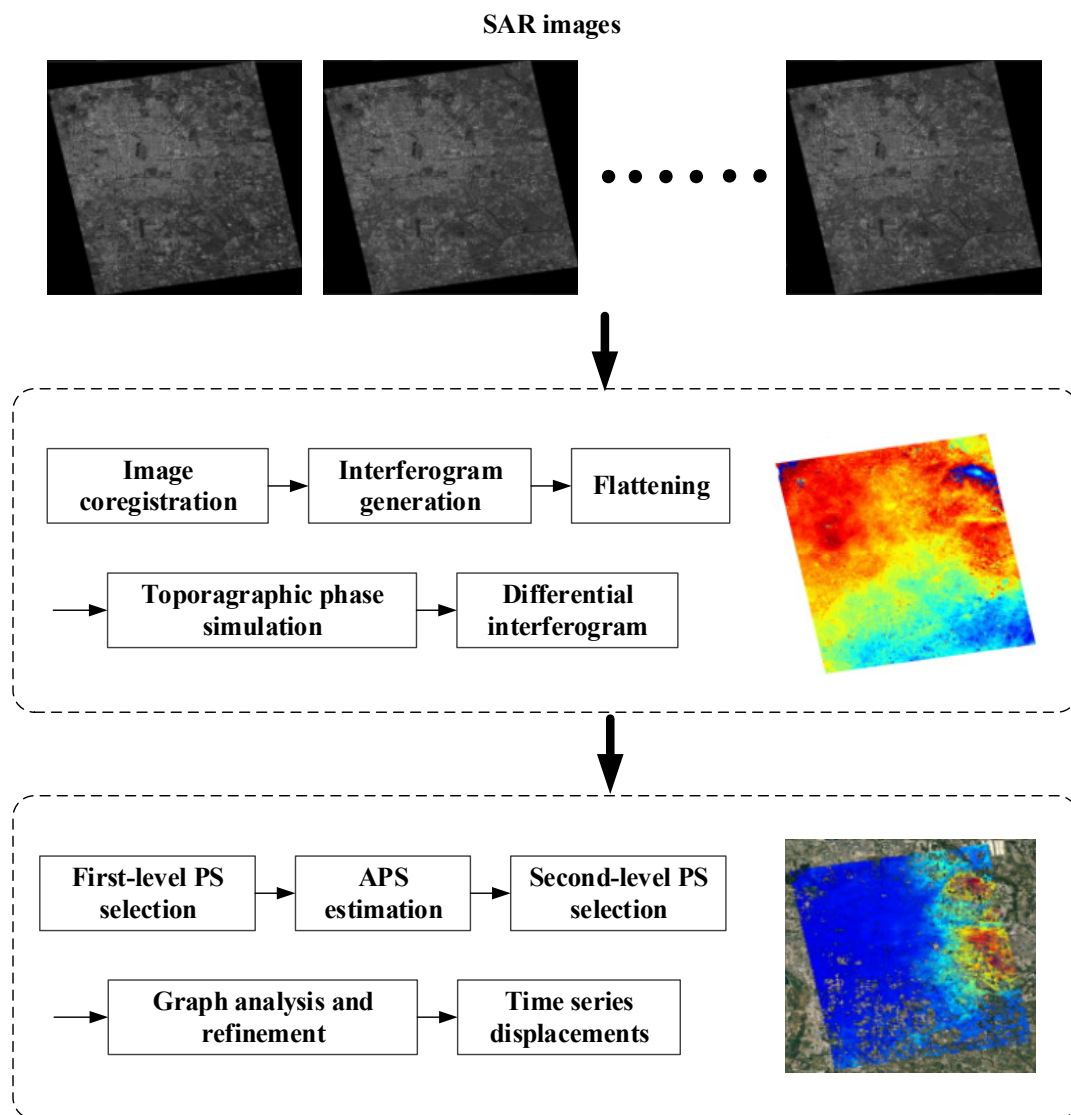


Figure 3. The flowchart of PS-InSAR processing steps.

4. Results and Discussion

4.1. InSAR-Derived Time Series Displacements

According to the methodology, the deformation rate map of the study area was obtained (Figure 4). The red points denote a negative deformation, thus indicating that the targets are far away from the satellite along the LOS. The blue points denote a positive deformation, thus indicating that the targets are close to the satellite along the LOS. A total of 950,789 PS were identified within 1250.5 km², leading to a PS density of 760 PS/km². The study area had large deformation rates, ranging from −117.4 to +5.1 mm/y between April 2010 and December 2019. The main land subsidence areas were in Chaoyang District and Tongzhou District. The InSAR measurement results were in good agreement with the leveling measurement results (Figure 5). The root mean square error (RMSE) was 4.0 mm/y.

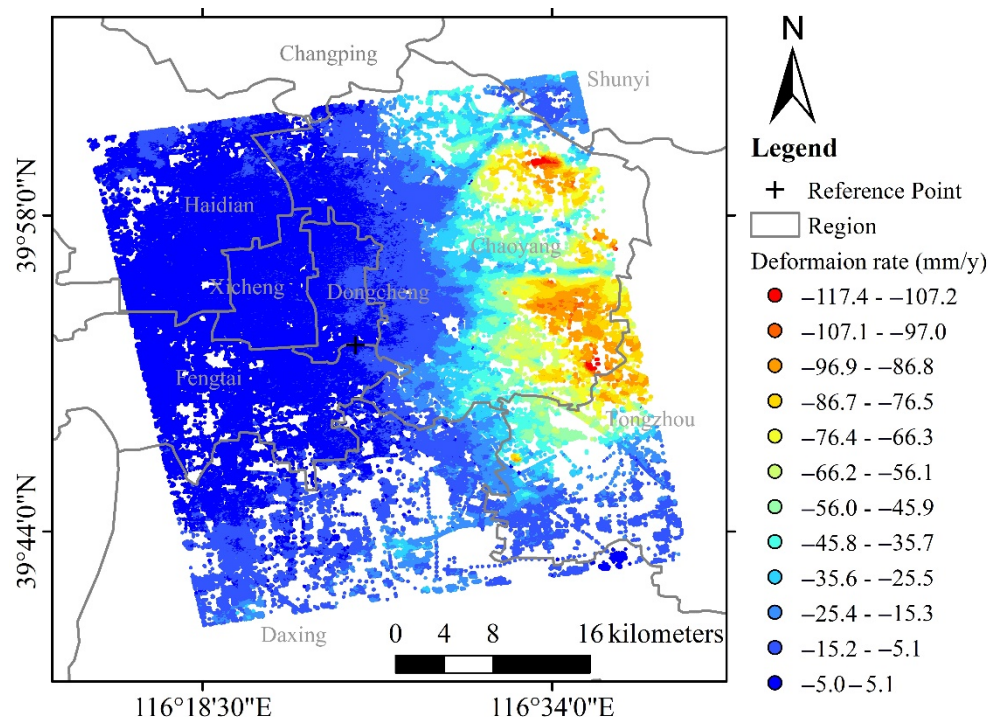


Figure 4. Deformation rate derived from PS-InSAR of TerraSAR-X stripmap images between April 2010 and December 2019.

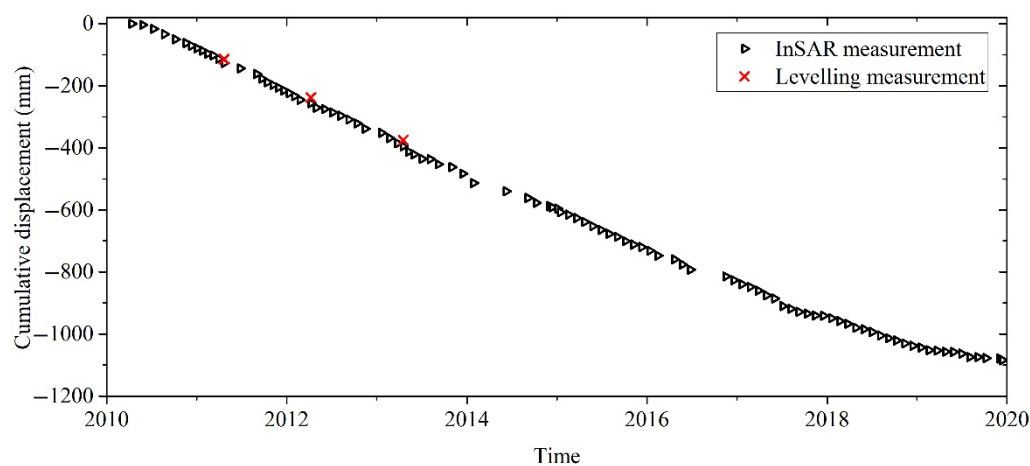


Figure 5. Time series displacement from the PS-InSAR measurement and levelling measurement.

4.2. Groundwater Levels

Changes in groundwater levels have a crucial impact on land subsidence. We need to focus on changes in groundwater levels and on the factors affecting changes in groundwater levels. The water supply and consumption structure need to be analyzed. The water supply structure of Beijing can be divided into five parts (Figure 6a). It should be noted that the proportion of groundwater decreased from 2010 to 2019. After the SNWDP in Beijing at the end of 2014, the decline of groundwater exploitation accelerated. By the end of 2019, the proportion fell to about 37%. In addition, the supply of recycle water increased year by year. The water consumption structure of Beijing can be divided into four parts (Figure 6b). Domestic water has always been the largest proportion. In addition, it has also been increasing slowly from the increase in resident population (Figure 7a). However, the relationship between domestic water and resident population is not linear. It may also be closely related to changes in people's water consumption. Environmental water has increased rapidly, quadrupling from 2010 to 2019, making it the second largest source

of water consumption. Moreover, environmental water has mainly been provided by recycled water due to its low water quality requirements [56]. There is a positive correlation between environmental water and public park area. Their correlation coefficient is 0.96, which is approximately linear (Figure 7b). It is worth noting that the Chinese government began air pollution control in 2013. The area of public parks increased rapidly from 2014, and environmental water consumption increased rapidly from 2015. There was a lag time of about one year between environmental water consumption and the area of public parks. However, both industrial and agricultural water have decreased year by year, especially agricultural water, which has decreased from 1.14 billion m^3 in 2010 to 0.37 billion m^3 in 2019.

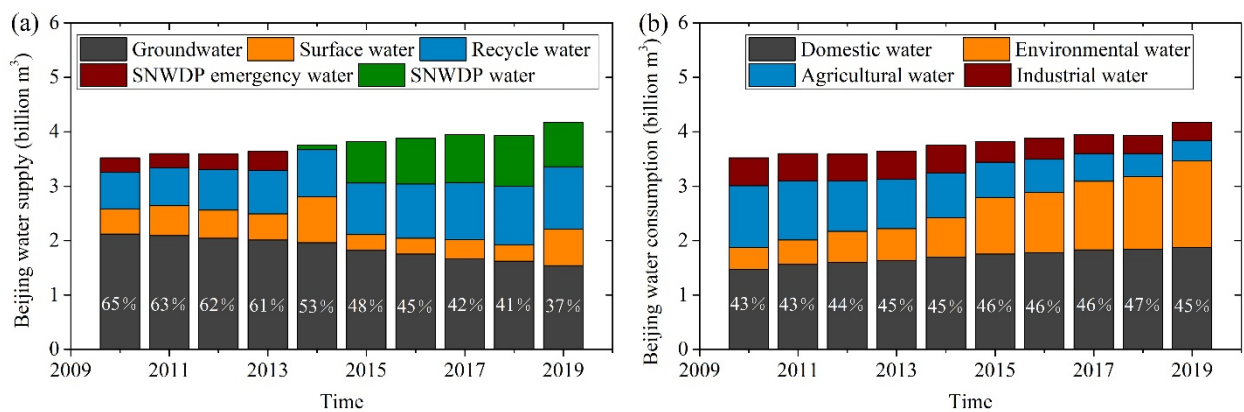


Figure 6. (a) The structure of total water supply. (b) The structure of total water consumption.

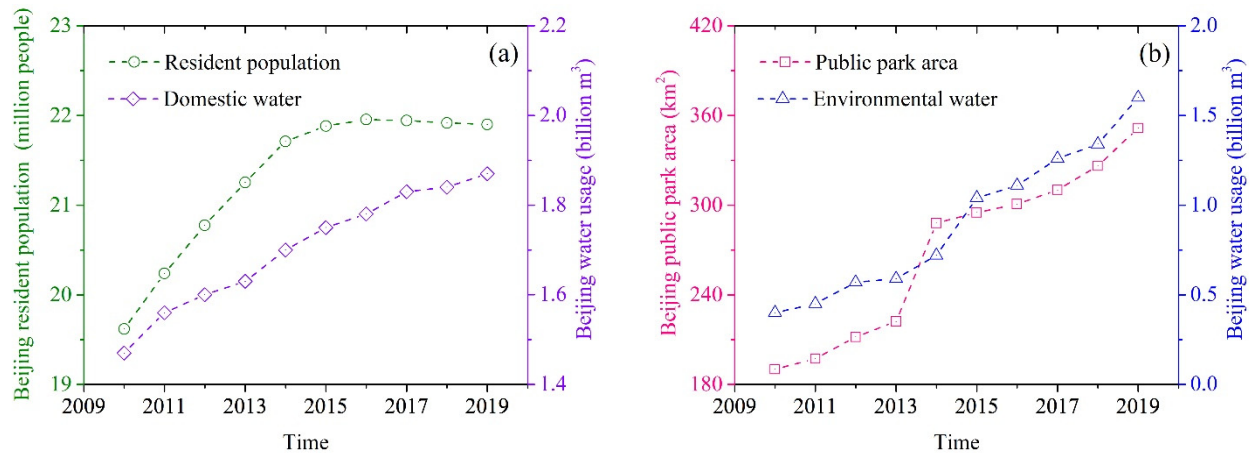


Figure 7. (a) The relation between resident population and domestic water. (b) The relation between public park area and environmental water.

The combination of surface water and groundwater is called the total water resource. Precipitation and its spatiotemporal distribution in Beijing have an important impact on the total amount of water resources [60]. The correlation coefficient between the total water resource and precipitation is very high (Figure 8), which is the same with previous studies [56,60]. Due to extremely increased precipitation, there was a brief rise in groundwater levels in 2012. The average precipitation in Beijing is 585 mm, which is much higher than the average values in 2010, 2011, 2013 and 2014. Decreases in precipitation aggravated the decline of groundwater levels, especially in the dry year of 2014 (Table 3). In addition, the SNWDP was completed on 7 December 2014, which transports water from southern China to Beijing. The average annual transportation is about $1.0 \times 10^9 m^3$ of water, which alleviates the impact of precipitation on groundwater to a certain extent. In addition to the influence of precipitation in 2012, the groundwater levels show a continuous decline from

2010 to 2015. The maximum level of average groundwater appeared at 25.75 m in 2015, which decreased by 0.83 m compared to that in 2010. It is worth noting that, from 2010 to 2019, the average groundwater levels reached a major turning point in 2016. The SNWDP water was continuously transported to Beijing, reversing declines in groundwater levels. Compared with the lowest point in 2015, the average groundwater level in 2019 increased by 3.04 m.

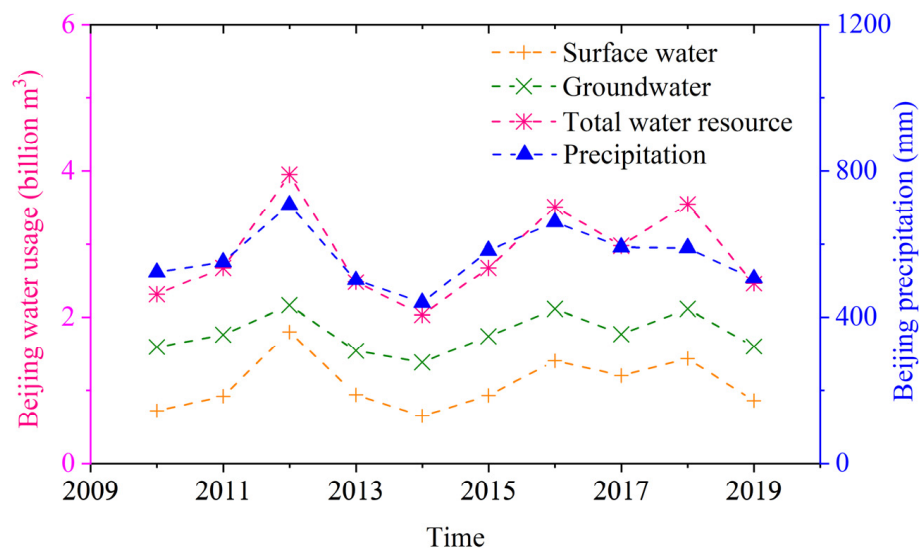


Figure 8. The relation between precipitation and total water resource.

Table 3. Average groundwater level, change in groundwater storage volume and water volume of SNWDP.

| Year | Average Groundwater Level (m) | Change in Groundwater Storage Volume ($\times 10^9 \text{ m}^3$) | Water Volume of the SNWDP Brought into Beijing ($\times 10^9 \text{ m}^3$) |
|------|-------------------------------|--|--|
| 2010 | 24.92 | −0.440 | |
| 2011 | 24.94 | −0.010 | |
| 2012 | 24.27 | +0.340 | |
| 2013 | 24.52 | −0.128 | |
| 2014 | 25.66 | −0.580 | 0.084 |
| 2015 | 25.75 | −0.050 | 0.881 |
| 2016 | 25.23 | +0.270 | 1.063 |
| 2017 | 24.97 | +0.130 | 1.077 |
| 2018 | 23.03 | +0.990 | 1.192 |
| 2019 | 22.71 | +0.160 | 0.985 |

Combined with changes in groundwater level, we analyzed the impacts on land subsidence. Land subsidence at three typical deformation centers are shown in Figure 9a–j. We found that land subsidence has changed significantly spatially from time. The changes in groundwater levels and land subsidence had a certain lag. After 2015, the groundwater levels rose year by year, leading to a slowdown in land subsidence in the following years, especially for the land subsidence of the Jinzhan deformation center (P1), Sanjianfang deformation center (P2) and Heizhuanghu deformation center (P3), which have decreased significantly. The time series displacement evolution process at each deformation center is shown in Figure 10. P1 reached a maximum deformation of -169.2 mm in 2012 and a minimum value of -93.9 mm in 2019. The deformation of P2 changed the most out of the three deformation centers, with a maximum value of -173.8 mm in 2013. Then, the deformation continued to decrease, with a minimum value of -56.3 mm in 2019. P3 also reached a maximum value of -169.1 mm in 2013, but the deformation suddenly began to

increase in 2017. Then, the deformation continued to decrease, with a minimum value of -54.1 mm in 2019.

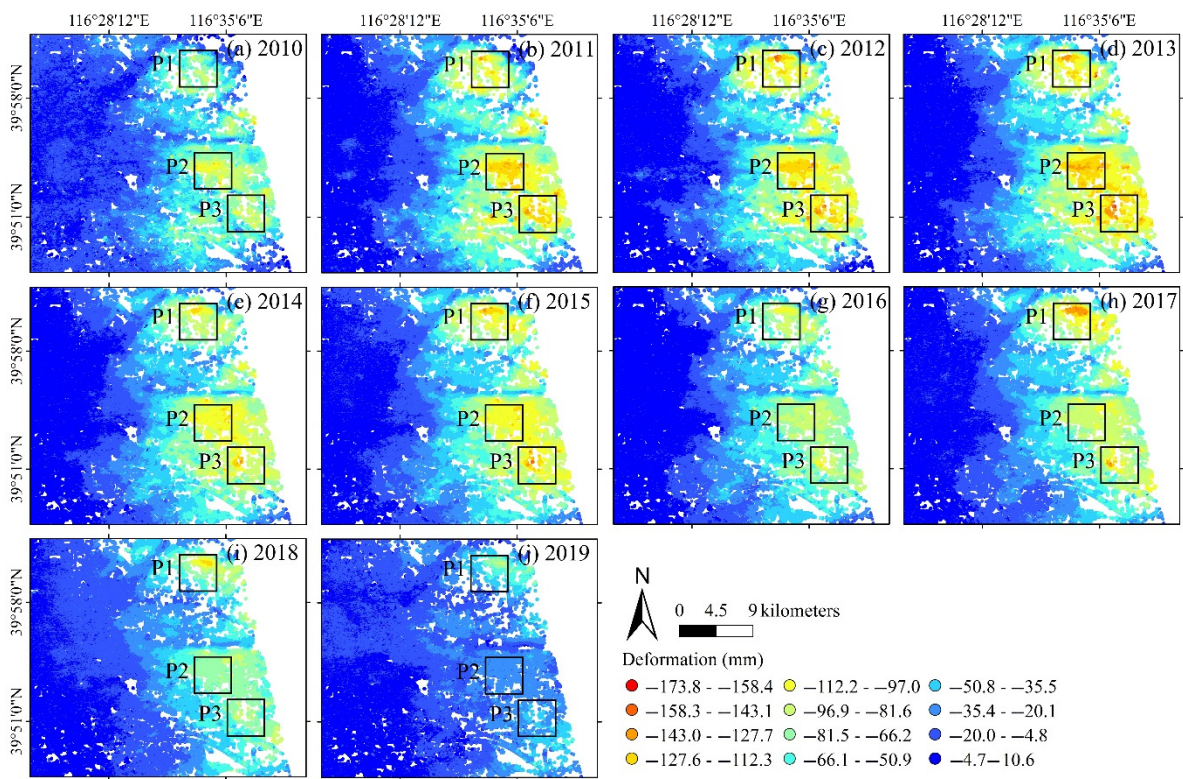


Figure 9. Deformation at different stages derived from PS-InSAR of TerraSAR-X stripmap images between April 2010 and December 2019.

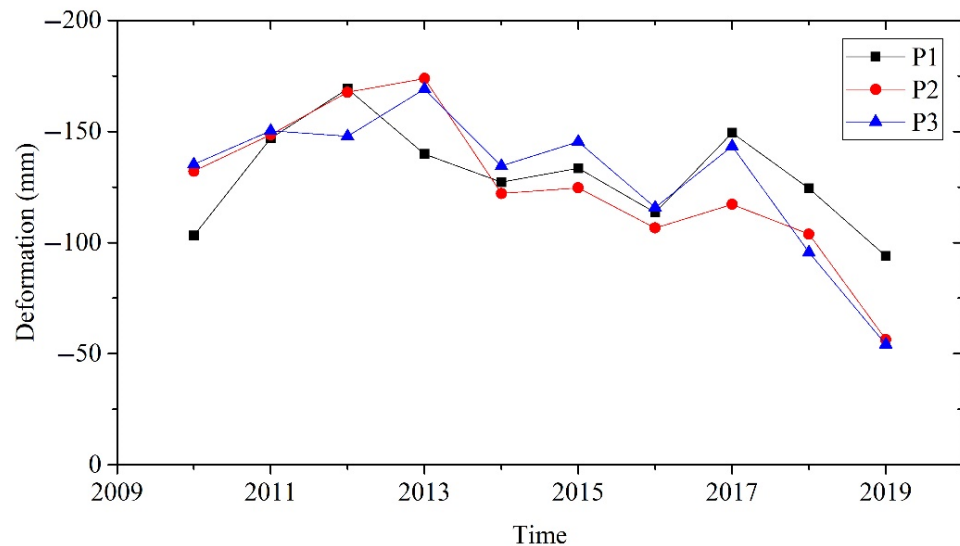


Figure 10. Time series displacement at three typical deformation centers.

Under the influence of changes in the water supply structure (the increase in SNWDP and recycle water, and the reduction in groundwater exploitation) and the optimization of the water consumption structure (recycled water for environmental water, and the reduction in agricultural water), groundwater levels began to rise after 2015. Furthermore, land subsidence values and area have decreased. The time series displacement of the three typical deformation centers show that land subsidence decreased in 2017 (about

two years after the start of SNWDP at the end of 2014). When the groundwater levels rose relative to the lowest point in 2015, land subsidence also decreased significantly. Different from the conclusion of Zhou et al. [52], this study found that reductions in the deformation rate lagged behind the time that the SNWDP needed to provide a water source by about two years. Based on Radarsat-2 and Sentinel-1 data from 2011 to 2018, Chen et al. [53] found that the time series displacement of typical deformation centers in Chaoyang and Shunyi districts also showed a decreasing trend two years after the start of SNWDP at the end of 2014. It has been proved that land subsidence does lag behind changes in groundwater levels. The SNWDP and precipitation changes affect land subsidence.

4.3. Human Activity

Land subsidence has a negative impact on the construction and operation of the urban rail transit system. Land subsidence may affect the stability of subways and their surrounding infrastructure. Therefore, it is important for their safety to identify land subsidence during construction and operation periods. Previous studies mostly focused on land subsidence in the operation periods [52]. Uneven land subsidence along subways was analyzed by using information such as the deformation rate.

This study focuses on analyzing land subsidence characteristics in the operation periods, as well as using long time series displacement to investigate land subsidence caused by underground soil excavation in the subway construction period. It not only analyzes the land subsidence distribution of the subway, but it also quantifies the change characteristics of the time series displacement in the whole period, from construction to operation. Figure 11 shows the deformation rate of the subway from 2010 to 2019. The average and maximum deformation rates of all subway lines were counted (Table 4). According to the statistical data, there are 15 subway lines in the study area and 6 subway lines with average deformation rates exceeding -5 mm/y. The results show that the Beijing subway lines are relatively stable, and the subway lines have large deformations only in the land subsidence section. Some subway lines in operation and under construction pass through the land subsidence area, especially the Heizhuanghu deformation center in Chaoyang District. The average deformation rate of Line 1 and Batong is the largest, reaching -22.5 mm/y, and the maximum deformation rate is -96.1 mm/y. For Line 6 and Line 7, the maximum deformation rates are -70.4 mm/y and -115.1 mm/y, respectively.

For the InSAR images, there are five subway lines of the construction period, namely Line 6, Line 7, Line 9, Line 14 and Line 16. We found that land subsidence was caused by underground soil excavation occurring in Line 6 and Line 7. The study area completely covers the first period of Line 6 (from Haidianwuluju station to Caofang station). The construction period of Line 6 was from December 2007 to December 2012. The study area completely covers the first period of Line 7 (from Beijing West station to Jiaohuachang station). The construction period of Line 7 was from 2010 to December 2014. As Line 6 and Line 7 pass through the Sanjianfang deformation center and the Heizhuanghu deformation center in Chaoyang District, many studies have discussed the characteristics of land subsidence along the subway. Duan et al. [48] analyzed the land subsidence characteristics of Line 6 from 2010 to 2018 by using TerraSAR-X data, focusing on the deformation gradient characteristics along the subway and the land subsidence evolution characteristics of different periods. Zhou et al. [52] investigated the spatial distribution characteristics of Beijing subway land subsidence by using RadarSAT-2 and Sentinel-1 data. However, there have been few studies concerning deformation changes in the subway construction and operation period, especially concerning whether the subway construction period caused land subsidence.

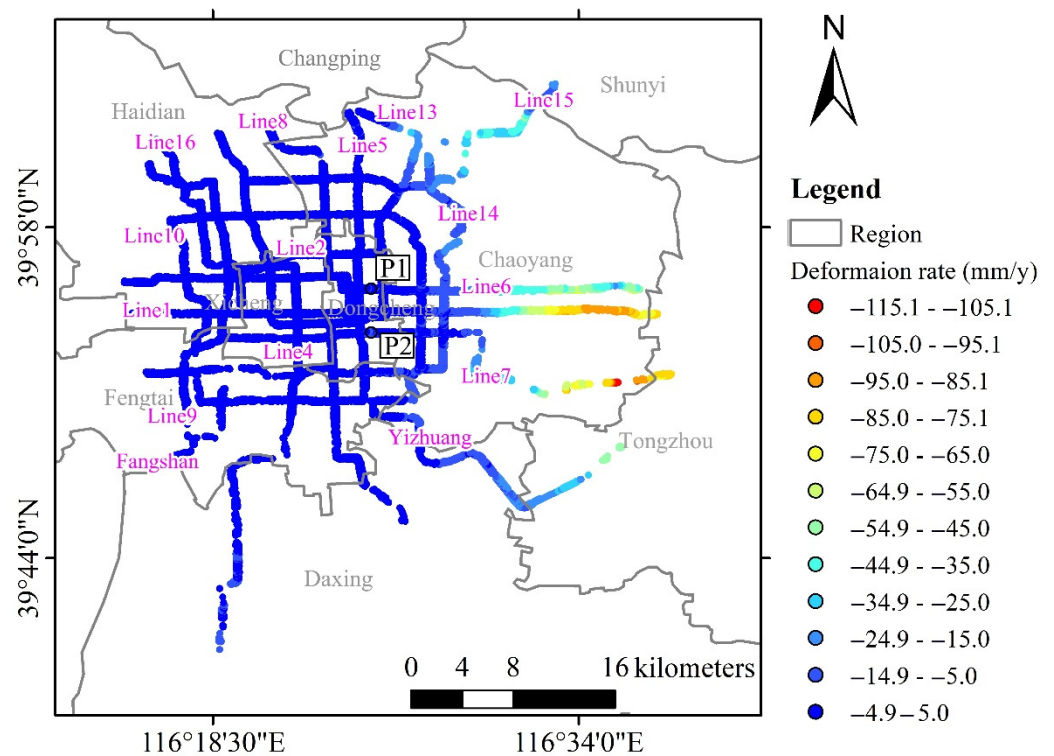


Figure 11. Deformation rates along Beijing subway lines.

Table 4. Properties of the subway lines in the study area.

| Name | First Opening Date | Average Deformation Rate (mm/y) | Maximum Deformation Rate (mm/y) |
|-------------------|--------------------|---------------------------------|---------------------------------|
| Line 1 and Batong | 1971 | -22.5 | -96.1 |
| Line 2 | 1971 | -0.1 | -6.8 |
| Line 4 | 2009 | 0.1 | -14.4 |
| Line 5 | 2007 | -1.4 | -7.9 |
| Line 6 | 2012 | -13.8 | -70.4 |
| Line 7 | 2014 | -10.0 | -115.1 |
| Line 8 | 2008 | -0.1 | -13.0 |
| Line 9 | 2011 | 1.5 | -4.1 |
| Line 10 | 2008 | -0.6 | -11.6 |
| Line 13 | 2002 | -1.8 | -26.6 |
| Line 14 | 2013 | -5.3 | -25.0 |
| Line 15 | 2010 | -8.2 | -48.2 |
| Line 16 | 2016 | 0.4 | -9.2 |
| Fangshan | 2010 | 1.4 | -2.9 |
| Yizhuang | 2010 | -11.8 | -50.9 |

We defined the “life cycle” of the subway as the construction period and the operation period. Land subsidence covers the construction period of Line 6 from April 2010 to December 2012 and the operation period of Line 6 from December 2012 to December 2019. The construction period of Line 7 was from April 2010 to December 2014, and the operation period of Line 7 was from December 2014 to December 2019. The monitoring time spans the entire life cycle of Line 6 and Line 7 from 2010 to 2019. During the construction period, we found that there was land subsidence about 500 m to the east of the Dongsi station on Line 6, and the time series displacement of typical P1 was drawn, as shown in Figure 12. The tunnel of the Dongsi station section was drilled by the drill and blast method. The tunnel has a height of 6.5 m, a width of 6.2 m and a depth of 33 m, mainly located in sand or gravel. The construction period is divided into four stages. In stages I–III of the

construction period, the displacement of P1 began in August 2010, sinking approximately linearly until the maximum displacement reached -23.3 mm in February 2012. Then, in stage IV of the construction period, there was a short uplift of about 8 mm over a period of about 7 months, and it finally stabilized. During the operation period of Line 6, P1 was relatively stable, but there was slow displacement of about 12 mm from July 2017 to December 2019. In addition, we also found that there was land subsidence during the construction period at Ciqikou station on Line 7, and the time series displacement of typical P2 was drawn, as shown in Figure 12. During the construction period of Line 7, the displacement of P2 slowly sank from April 2010 to September 2011, reaching -9.6 mm. Then, the displacement began to accelerate until January 2013, with a displacement of about 48 mm in just 16 months. Finally, it tended to be stable, and there was no obvious displacement during the operation period.

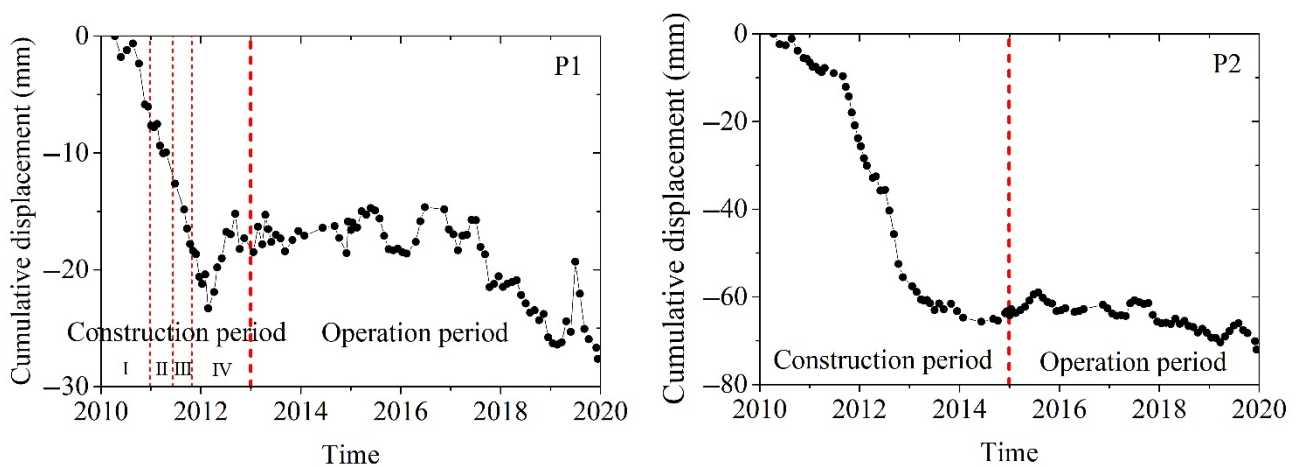


Figure 12. Time series displacement of P1 and P2. I: small pilot tunnel construction stage; II: beam and column construction stage; III: arch buckle construction stage; IV: earth excavation and main structure construction stage.

Furthermore, the deformation rate profiles of Line 6 and Line 7 are shown in Figure 13. The deformation rate of Line 6 exceeded -5 mm/y at the mileage of 19.3 km (Hujialou station) and reached a maximum deformation rate of 36.4 mm/y at the mileage of 28.5 km (Dalianpo station). It is worth noting that, within the mileage of 28.5 km to 32 km (Caofang station), the deformation rate decreased (the deformation rate at the mileage of 30.9 km (Changying station) was 23.8 mm/y) and then increased, resulting in an obvious uneven subsidence. The deformation rate of Line 7 was -5 mm/y at the mileage of 14.8 km (Huagong station), and the maximum deformation rate was -112.5 mm/y at the mileage of 27.6 km (Heizhuanghu station). There was significant uneven land subsidence at the mileage of 9 km (Ciqikou station), with a deformation rate of -9.0 mm/y, which was the same as that at P2 (Figure 11).

Previous studies mostly focused on slow linear land subsidence [54]. Uneven and nonlinear land subsidence often causes great harm, especially underground soil excavation during the construction period, resulting in rapid displacement of the ground around the subway in a short time. These uneven and nonlinear land subsidence may cause serious hazards, such as ground collapse and house cracking. Therefore, it is not only necessary to pay attention to the spatial distribution of land subsidence, but also to analyze the changes in time series displacement during subway construction. It can be seen from the results that the long time series InSAR displacement can be used as important information on land subsidence during the underground engineering construction period.

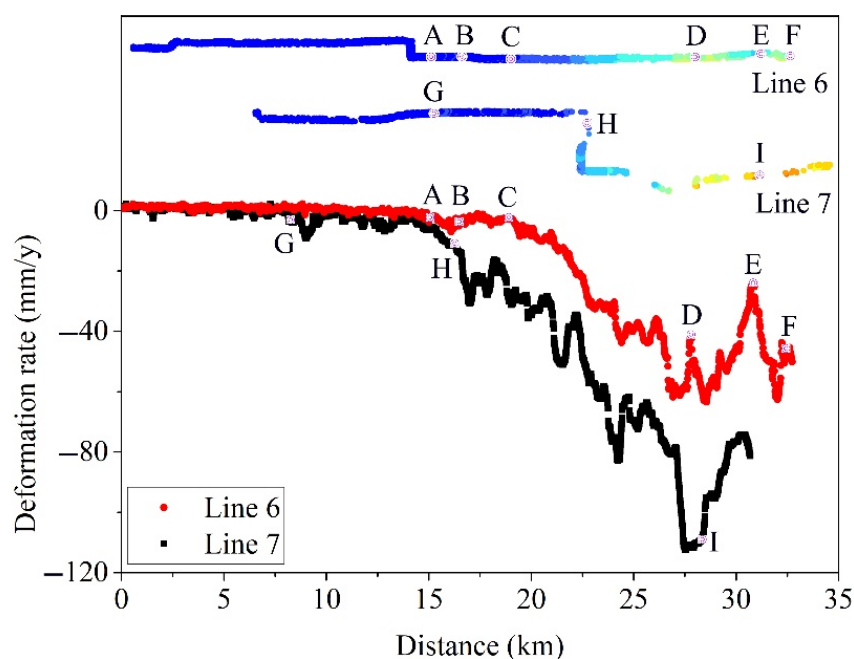


Figure 13. Deformation rate profile of Line 6 and Line 7. The x -axis represents the distance from the west endpoint to the east endpoint. (A) Dongsi Station, (B) Chaoyangmen Station, (C) Hujialou Station, (D) Dalianpo Station, (E) Changying Station, (F) Caofang Station, (G) Ciqikou Station, (H) Huagong Station, (I) Heizhuanghu Station.

4.4. Surface Geology

The Quaternary sedimentary layer is the main shrinkage layer of land subsidence in the study area. The thickness and differential changes from the Quaternary sedimentary layer are important geological background for the emergence and development of uneven land subsidence [2]. The thickness of the Quaternary sedimentary layer varies greatly. Fine sediment areas are more likely to cause land subsidence. Unfortunately, the whole northeast of Beijing is in fine sediments, which provides a potential risk for the development of sedimentation.

In addition, decreases in groundwater levels reduce pore water pressure, resulting in increases in the effective stress of soil. The water bearing the sand layer shows elastic deformation. When the water level recovers, the deformation of water bearing the sand layer rebounds to a certain extent, whereas the weakly permeable layer mainly shows plastic deformation and permanent deformation. In the Section 4.2, the groundwater level in Beijing began to rise after 2015. Due to the thickness difference in the spatial distribution of the aquifer sand layer and the weakly permeable layer, there are also differences in deformation, which can easily cause uneven land subsidence [37]. Due to the lack of detailed geological data, subsidence-driving mechanisms have not been deeply studied. We hope to study subsidence-driving mechanisms through lithostratigraphic reconstruction and further Lithological Ratio (LR) analysis [16] in the future.

4.5. Active Faults

Active faults affect the sedimentary process, leading to differences in the spatial distribution of Quaternary sedimentary layer thickness, which provides the geological conditions for inducing uneven land subsidence. The main active faults of the study area include Gaoliying Fault (F2) and Shunyi Fault (F3) (Figure 14a). The data of Shun 4 and Shun 5 drill holes in the upper and lower plates of Shunyi fault show that the same sedimentary strata on both sides of the fault differ by more than 200 m (Figure 14b). The typical deformation rate profile line B-B' was drawn, passing through active faults (Figure 14c). Its location is shown in Figure 14a. Section B-B' passes through Gaoliying fault and Shunyi fault. The maximum differential deformation rate of Gaoliying fault is

13.6 mm/y. In Shunyi fault, the maximum difference of the deformation rate is 50.8 mm/y. In the area where the active fault passes through, the deformation rate profile shows a clear turning point or a sudden change, and uneven land subsidence is distributed on both sides of the fault. Our results regarding active faults agree well with previous studies [43,57].

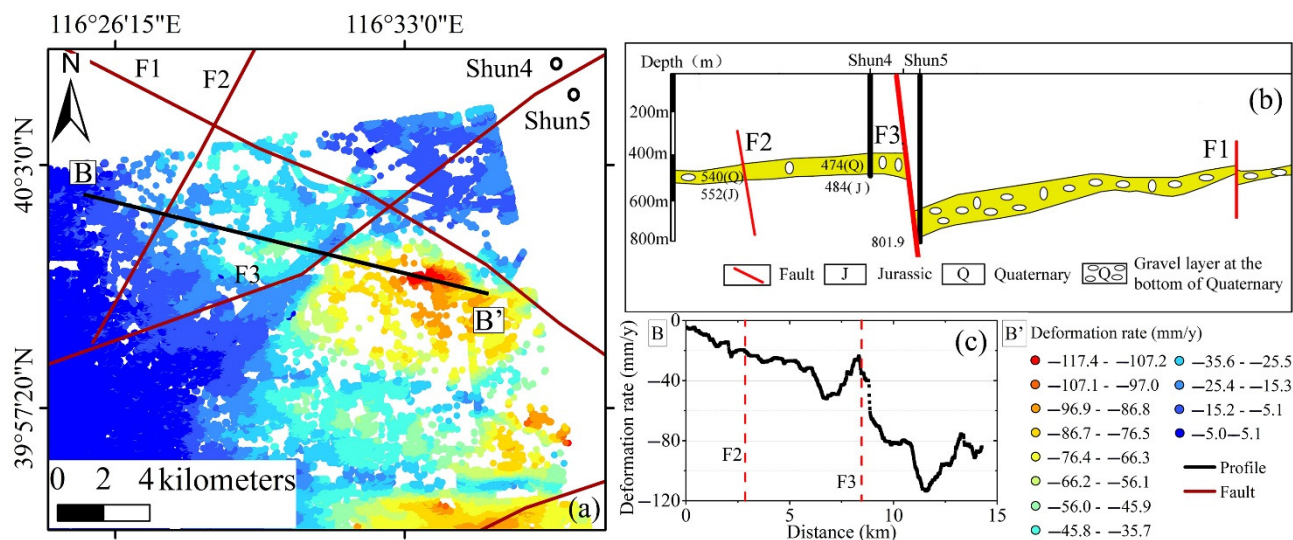


Figure 14. (a) Distribution of land subsidence in active fault areas. (b) Profile of the Shunyi fault. (derived from [57]). (c) Profiles of deformation rates on both sides of the faults (B-B').

5. Conclusions

This study presents a PS-InSAR analysis of 100 TerraSAR-X stripmap images, which were used to monitor the decadal evolution of land subsidence in Beijing. Water resources and historic climate and urban construction data were compiled from 2010 to 2019 to analyze changes in groundwater levels, human activity, surface geology, active fault factors and land subsidence patterns. The following conclusions were drawn:

- (1) In the past 10 years, Beijing's water supply and consumption structure have undergone great changes. Increases in SNWDP water and recycled water have gradually improved the current situation of water resources, making the groundwater level increase year by year. As public park area expanded, environmental water consumption increased year by year. Although the resident population of Beijing has decreased, domestic water consumption has increased year by year due to changes in people's water usage. With changes in the water supply structure (the increase in SNWDP and recycled water, and the reduction in groundwater exploitation) and the optimization of water consumption (recycled water for environmental water, and the reduction in agricultural water), groundwater levels began to rise after 2015.
- (2) Groundwater levels have begun to rise, leading to decreases in deformation rates and areas of land subsidence. In discussions of the time series displacement of three deformation centers, we found that land subsidence has decreased since 2017, and reductions in deformation rate lagged behind the time that the SNWDP needed to provide a water source by about two years. In fact, land subsidence lagged behind changes in groundwater levels.
- (3) Uneven and nonlinear land subsidence often causes greater harm. We found that, due to underground soil excavation, the ground around the subway subsided rapidly in a short time during the construction periods of Line 6 and Line 7. About 500 m to the east of the Dongsi station of Line 6, the displacement was -23.3 mm from August 2010 to February 2012. Ciqikou station of Line 7 sank about 48 mm in just 16 months from September 2011 to January 2013. During the construction period, uneven and nonlinear land subsidence needs to be paid more attention.

- (4) Active faults affect the sedimentary process, leading to differences in the spatial distribution of Quaternary sedimentary layer thickness, which provides geological conditions for inducing uneven land subsidence. The land subsidence profile shows a clear turning point or sudden change on both sides of the Shunyi fault, and uneven land subsidence is distributed on both sides of the fault.

Author Contributions: Conceptualization, Z.B. and Y.W.; methodology, Z.B.; software, Z.B.; validation, Z.B.; formal analysis, Z.B.; investigation, Z.B.; resources, Z.B.; writing—original draft preparation, Z.B.; writing—review and editing, Z.B. and T.B.; visualization, Z.B.; supervision, Z.B.; project administration, Y.W.; funding acquisition, Y.W. All authors have read and agreed to the published version of the manuscript.

Funding: This research was funded by the Innovation Team Building Support Program of Beijing Municipal Education Commission (grant number IDHT20190501) and the key international cooperation projects of the National Natural Science Foundation of China (grant number 61860206013).

Acknowledgments: We thank the German Aerospace Center (DLR) for their efforts in developing and distributing the remotely sensed SAR data.

Conflicts of Interest: The authors declare no conflict of interest.

References

- Herrera-García, G.; Ezquerro, P.; Tomás, R.; Béjar-Pizarro, M.; López-Vinielles, J.; Rossi, M.; Mateos, R.M.; Carreón-Freyre, D.; Lambert, J.; Teatini, P.; et al. Mapping the global threat of land subsidence. *Science* **2021**, *371*, 34–36. [[CrossRef](#)] [[PubMed](#)]
- Gong, H.; Pan, Y.; Zheng, L.; Li, X.; Zhu, L.; Zhang, C.; Huang, Z.; Li, Z.; Wang, H.; Zhou, C. Long-term groundwater storage changes and land subsidence development in the North China Plain (1971–2015). *Appl. Hydrogeol.* **2018**, *26*, 1417–1427. [[CrossRef](#)]
- Chen, J.; Knight, R.; Zebker, H.A.; Schreüder, W.A. Confined aquifer head measurements and storage properties in the San Luis Valley, Colorado, from spaceborne InSAR observations. *Water Resour. Res.* **2016**, *52*, 3623–3636. [[CrossRef](#)]
- Hu, X.; Lu, Z.; Wang, T. Characterization of Hydrogeological Properties in Salt Lake Valley, Utah, using InSAR. *J. Geophys. Res. Earth Surf.* **2018**, *123*, 1257–1271. [[CrossRef](#)]
- Cigna, F.; Tapete, D. Present-day land subsidence rates, surface faulting hazard and risk in Mexico City with 2014–2020 Sentinel-1 IW InSAR. *Remote Sens. Environ.* **2021**, *253*, 112161. [[CrossRef](#)]
- Du, Z.; Ge, L.; Ng, A.H.M.; Zhu, Q.; Yang, X.; Li, L. Correlating the subsidence pattern and land use in Bandung, Indonesia with both Sentinel-1/2 and ALOS-2 satellite images. *Int. J. Appl. Earth Obs. Geoinf.* **2018**, *67*, 54–68. [[CrossRef](#)]
- Najafabadi, R.M.; Ramesht, M.H.; Ghazi, I.; Khajedin, S.J.; Seif, A.; Nohegar, A.; Mahdavi, A. Identification of natural hazards and classification of urban areas by TOPSIS model (case study: Bandar Abbas city, Iran). *Geomat. Nat. Hazards Risk* **2016**, *7*, 85–100. [[CrossRef](#)]
- El Bastawesy, M.; Cherif, O.H.; Sultan, M. The geomorphological evidences of subsidence in the Nile Delta: Analysis of high resolution topographic DEM and multi-temporal satellite images. *J. Afr. Earth Sci.* **2017**, *136*, 252–261. [[CrossRef](#)]
- Teatini, P.; Baù, D.; Gambolati, G. Water-gas dynamics and coastal land subsidence over Chioggia Mare field, northern Adriatic Sea. *Appl. Hydrogeol.* **2000**, *8*, 462–479. [[CrossRef](#)]
- Brambati, A.; Carbognin, L.; Quaia, T.; Teatini, P.; Tosi, A.L. The Lagoon of Venice: Geological setting, evolution and land subsidence. *Episodes* **2003**, *26*, 264–268. [[CrossRef](#)]
- Teatini, P.; Ferronato, M.; Gambolati, G.; Gonella, M. Groundwater pumping and land subsidence in the Emilia-Romagna coastland, Italy: Modeling the past occurrence and the future trend. *Water Resour. Res.* **2006**, *42*, 1–9. [[CrossRef](#)]
- Tosi, L.; Teatini, P.; Strozzi, T. Natural versus anthropogenic subsidence of Venice. *Sci. Rep.* **2013**, *3*, 2710. [[CrossRef](#)] [[PubMed](#)]
- Aucelli, P.P.C.; Di Paola, G.; Incontri, P.; Rizzo, A.; Vilaro, G.; Benassai, G.; Buonocore, B.; Pappone, G. Coastal Inundation Risk Assessment Due to Subsidence and Sea Level Rise in a Mediterranean Alluvial Plain (Volturno Coastal Plain—Southern Italy). *Estuar. Coast. Shelf Sci.* **2017**, *198*, 597–609. [[CrossRef](#)]
- Matano, F.; Sacchi, M.; Vigliotti, M.; Ruberti, D. Subsidence Trends of Volturno River Coastal Plain (Northern Campania, Southern Italy) Inferred by SAR Interferometry Data. *Geosciences* **2018**, *8*, 8. [[CrossRef](#)]
- Busico, G.; Buffardi, C.; Ntona, M.M.; Vigliotti, M.; Colombani, N.; Mastrocicco, M.; Ruberti, D. Actual and Forecasted Vulnerability Assessment to Seawater Intrusion via GALDIT-SUSI in the Volturno River Mouth (Italy). *Remote Sens.* **2021**, *13*, 3632. [[CrossRef](#)]
- Buffardi, C.; Barbato, R.; Vigliotti, M.; Mandolini, A.; Ruberti, D. The Holocene Evolution of the Volturno Coastal Plain (Northern Campania, Southern Italy): Implications for the Understanding of Subsidence Patterns. *Water* **2021**, *13*, 2692. [[CrossRef](#)]
- Herrera, G.; Fernández, J.A.; Tomás, R.; Cooksley, G.; Mulas, J. Advanced interpretation of subsidence in Murcia (SE Spain) using A-DInSAR data—Modelling and validation. *Nat. Hazards Earth Syst. Sci.* **2009**, *9*, 647–661. [[CrossRef](#)]

18. Bonì, R.; Herrera, G.; Meisina, C.; Notti, D.; Béjar-Pizarro, M.; Zucca, F.; Gonzalez, P.J.; Palano, M.; Tomás, R.; Fernandez, J.; et al. Twenty-year advanced DInSAR analysis of severe land subsidence: The Alto Guadalentín Basin (Spain) case study. *Eng. Geol.* **2015**, *198*, 40–52. [[CrossRef](#)]
19. Muntendam-Bos, A.G.; Kleuskens, M.H.P.; Bakr, M.; de Lange, G.; Fokker, P.A. Unraveling shallow causes of subsidence. *Geophys. Res. Lett.* **2009**, *36*. [[CrossRef](#)]
20. Weststrate, T.W. Urban Land Subsidence in the Netherlands. Master's Thesis, Radboud University, Nijmegen, The Netherlands, 9–11 July 2018.
21. Ge, L.; Li, X.; Chang, H.-C.; Ng, A.H.M.; Zhang, K.; Hu, Z. Impact of ground subsidence on the Beijing–Tianjin high-speed railway as mapped by radar interferometry. *Ann. GIS* **2010**, *16*, 91–102. [[CrossRef](#)]
22. Yang, M.; Yang, T.; Zhang, L.; Lin, J.; Qin, X.; Liao, M. Spatio-Temporal Characterization of a Reclamation Settlement in the Shanghai Coastal Area with Time Series Analyses of X-, C-, and L-Band SAR Datasets. *Remote Sens.* **2018**, *10*, 329. [[CrossRef](#)]
23. Qu, F.; Zhang, Q.; Lu, Z.; Zhao, C.; Yang, C.; Zhang, J. Land subsidence and ground fissures in Xi'an, China 2005–2012 revealed by multi-band InSAR time-series analysis. *Remote Sens. Environ.* **2014**, *155*, 366–376. [[CrossRef](#)]
24. Jiang, H.; Balz, T.; Cigna, F.; Tapete, D. Land Subsidence in Wuhan Revealed Using a Non-Linear PSInSAR Approach with Long Time Series of COSMO-SkyMed SAR Data. *Remote Sens.* **2021**, *13*, 1256. [[CrossRef](#)]
25. Ai, J.; Mao, Y.; Luo, Q.; Jia, L.; Xing, M. SAR Target Classification Using the Multikernel-Size Feature Fusion-Based Convolutional Neural Network. *IEEE Trans. Geosci. Remote Sens.* **2022**, *60*, 5214313. [[CrossRef](#)]
26. Ai, J.; Tian, R.; Luo, Q.; Jin, J.; Tang, B. Multi-Scale Rotation-Invariant Haar-Like Feature Integrated CNN-Based Ship Detection Algorithm of Multiple-Target Environment in SAR Imagery. *IEEE Trans. Geosci. Remote Sens.* **2019**, *57*, 10070–10087. [[CrossRef](#)]
27. Minh, D.H.T.; Hanssen, R.; Rocca, F. Radar Interferometry: 20 Years of Development in Time Series Techniques and Future Perspectives. *Remote Sens.* **2020**, *12*, 1364. [[CrossRef](#)]
28. Mora, O.; Lanari, R.; Mallorqui, J.J.; Berardino, P.; Sansosti, E. Landslide failures detection and mapping using Synthetic Aperture Radar: Past, present and future. *Earth Sci. Rev.* **2021**, *216*, 103574. [[CrossRef](#)]
29. Ferretti, A.; Prati, C.; Rocca, F. Nonlinear Subsidence Rate Estimation Using permanent scatterers in differential SAR interferometry. *IEEE Trans. Geosci. Remote Sens.* **2000**, *38*, 2202–2212. [[CrossRef](#)]
30. Berardino, P.; Fornaro, G.; Lanari, R.; Sansosti, E. A new algorithm for surface deformation monitoring based on small baseline differential SAR interferograms. *IEEE Trans. Geosci. Remote Sens.* **2002**, *40*, 2375–2383. [[CrossRef](#)]
31. Zhang, L.; Lu, Z.; Ding, X.; Jung, H.-S.; Feng, G.; Lee, C.-W. Mapping ground surface deformation using temporarily coherent point SAR interferometry: Application to Los Angeles Basin. *Remote Sens. Environ.* **2012**, *117*, 429–439. [[CrossRef](#)]
32. Perissin, D.; Wang, T. Repeat-Pass SAR Interferometry with Partially Coherent Targets. *IEEE Trans. Geosci. Remote. Sens.* **2011**, *50*, 271–280. [[CrossRef](#)]
33. Zhu, X.X.; Wang, Y.; Montazeri, S.; Ge, N. A Review of Ten-Year Advances of Multi-Baseline SAR Interferometry Using TerraSAR-X Data. *Remote Sens.* **2018**, *10*, 1374. [[CrossRef](#)]
34. Chen, B.; Gong, H.; Li, X.; Lei, K.; Zhang, Y.; Li, J.; Gu, Z.; Dang, Y. Spatial-temporal characteristics of land subsidence corresponding to dynamic groundwater funnel in Beijing Municipality, China. *Chin. Geogr. Sci.* **2011**, *21*, 753–764. [[CrossRef](#)]
35. Ng, A.H.-M.; Ge, L.; Li, X.; Zhang, K. Monitoring ground deformation in Beijing, China with persistent scatterer SAR interferometry. *J. Geod.* **2012**, *86*, 375–392. [[CrossRef](#)]
36. Hu, B.; Wang, H.-S.; Sun, Y.-L.; Hou, J.-G.; Liang, J. Long-Term Land Subsidence Monitoring of Beijing (China) Using the Small Baseline Subset (SBAS) Technique. *Remote Sens.* **2014**, *6*, 3648–3661. [[CrossRef](#)]
37. Zhu, L.; Gong, H.; Li, X.; Wang, R.; Chen, B.; Dai, Z.; Teatini, P. Land subsidence due to groundwater withdrawal in the northern Beijing plain, China. *Eng. Geol.* **2015**, *193*, 243–255. [[CrossRef](#)]
38. Chen, M.; Tomás, R.; Li, Z.; Motagh, M.; Li, T.; Hu, L.; Gong, H.; Li, X.; Yu, J.; Gong, X. Imaging Land Subsidence Induced by Groundwater Extraction in Beijing (China) Using Satellite Radar Interferometry. *Remote Sens.* **2016**, *8*, 468. [[CrossRef](#)]
39. Gao, M.; Gong, H.; Chen, B.; Zhou, C.; Chen, W.; Liang, Y.; Shi, M.; Si, Y. InSAR time-series investigation of long-term ground displacement at Beijing Capital International Airport, China. *Tectonophysics* **2016**, *691*, 271–281. [[CrossRef](#)]
40. Zhang, Y.; Wu, H.; Kang, Y.; Zhu, C. Ground Subsidence in the Beijing-Tianjin-Hebei Region from 1992 to 2014 Revealed by Multiple SAR Stacks. *Remote Sens.* **2016**, *8*, 675. [[CrossRef](#)]
41. Chen, B.; Gong, H.; Li, X.; Lei, K.; Zhu, L.; Gao, M.; Zhou, C. Characterization and causes of land subsidence in Beijing, China. *Int. J. Remote Sens.* **2017**, *38*, 808–826. [[CrossRef](#)]
42. Zhou, C.; Gong, H.; Chen, B.; Li, J.; Gao, M.; Zhu, F.; Chen, W.; Liang, Y. InSAR Time-Series Analysis of Land Subsidence under Different Land Use Types in the Eastern Beijing Plain, China. *Remote Sens.* **2017**, *9*, 380. [[CrossRef](#)]
43. Gao, M.; Gong, H.; Chen, B.; Li, X.; Zhou, C.; Shi, M.; Si, Y.; Chen, Z.; Duan, G. Regional Land Subsidence Analysis in Eastern Beijing Plain by InSAR Time Series and Wavelet Transforms. *Remote Sens.* **2018**, *10*, 365. [[CrossRef](#)]
44. Yang, Q.; Ke, Y.; Zhang, D.; Chen, B.; Gong, H.; Lv, M.; Zhu, L.; Li, X. Multi-Scale Analysis of the Relationship between Land Subsidence and Buildings: A Case Study in an Eastern Beijing Urban Area Using the PS-InSAR Technique. *Remote Sens.* **2018**, *10*, 1006. [[CrossRef](#)]
45. Zhou, C.; Gong, H.; Zhang, Y.; Warner, T.A.; Wang, C. Spatiotemporal Evolution of Land Subsidence in the Beijing Plain 2003–2015 Using Persistent Scatterer Interferometry (PSI) with Multi-Source SAR Data. *Remote Sens.* **2018**, *10*, 552. [[CrossRef](#)]

46. Gao, M.; Gong, H.; Li, X.; Chen, B.; Zhou, C.; Shi, M.; Guo, L.; Chen, Z.; Ni, Z.; Duan, G. Land Subsidence and Ground Fissures in Beijing Capital International Airport (BCIA): Evidence from Quasi-PS InSAR Analysis. *Remote Sens.* **2019**, *11*, 1466. [[CrossRef](#)]
47. Zhou, C.; Lan, H.; Gong, H.; Zhang, Y.; Warner, T.A.; Clague, J.J.; Wu, Y. Reduced rate of land subsidence since 2016 in Beijing, China: Evidence from Tomo-PSInSAR using RadarSAT-2 and Sentinel-1 datasets. *Int. J. Remote Sens.* **2020**, *41*, 1259–1285. [[CrossRef](#)]
48. Duan, L.; Gong, H.; Chen, B.; Zhou, C.; Lei, K.; Gao, M.; Yu, H.; Cao, Q.; Cao, J. An Improved Multi-Sensor MTI Time-Series Fusion Method to Monitor the Subsidence of Beijing Subway Network During the Past 15 Years. *Remote Sens.* **2020**, *12*, 2125. [[CrossRef](#)]
49. Shi, M.; Gong, H.; Gao, M.; Chen, B.; Zhang, S.; Zhou, C. Recent Ground Subsidence in the North China Plain, China, Revealed by Sentinel-1A Datasets. *Remote Sens.* **2020**, *12*, 3579. [[CrossRef](#)]
50. Lyu, M.; Ke, Y.; Li, X.; Zhu, L.; Guo, L.; Gong, H. Detection of Seasonal Deformation of Highway Overpasses Using the PS-InSAR Technique: A Case Study in Beijing Urban Area. *Remote Sens.* **2020**, *12*, 3071. [[CrossRef](#)]
51. Zhao, X.; Chen, B.; Gong, H.; Zhou, C.; Li, X.; Lei, K.; Ke, Y. Land subsidence along the Beijing–Tianjin Intercity Railway during the period of the South-to-North Water Diversion Project. *Int. J. Remote Sens.* **2020**, *41*, 4447–4469. [[CrossRef](#)]
52. Zhou, C.; Gong, H.; Chen, B.; Gao, M.; Cao, Q.; Cao, J.; Duan, L.; Zuo, J.; Shi, M. Land Subsidence Response to Different Land Use Types and Water Resource Utilization in Beijing-Tianjin-Hebei, China. *Remote Sens.* **2020**, *12*, 457. [[CrossRef](#)]
53. Chen, B.; Gong, H.; Chen, Y.; Li, X.; Zhou, C.; Lei, K.; Zhu, L.; Duan, L.; Zhao, X. Land subsidence and its relation with groundwater aquifers in Beijing Plain of China. *Sci. Total Environ.* **2020**, *735*, 139111. [[CrossRef](#)] [[PubMed](#)]
54. Chen, B.; Gong, H.; Chen, Y.; Lei, K.; Zhou, C.; Si, Y.; Li, X.; Pan, Y.; Gao, M. Investigating land subsidence and its causes along Beijing high-speed railway using multi-platform InSAR and a maximum entropy model. *Int. J. Appl. Earth Obs. Geoinf. ITC J.* **2021**, *96*, 102284. [[CrossRef](#)]
55. Wang, Y.; Bai, Z.; Zhang, Y.; Qin, Y.; Lin, Y.; Li, Y.; Shen, W. Using TerraSAR X-Band and Sentinel-1 C-Band SAR Interferometry for Deformation Along Beijing-Tianjin Intercity Railway Analysis. *IEEE J. Sel. Top. Appl. Earth Obs. Remote Sens.* **2021**, *14*, 4832–4841. [[CrossRef](#)]
56. Du, Z.; Ge, L.; Ng, A.H.-M.; Lian, X.; Zhu, Q.; Horgan, F.G.; Zhang, Q. Analysis of the impact of the South-to-North water diversion project on water balance and land subsidence in Beijing, China between 2007 and 2020. *J. Hydrol.* **2021**, *603*, 126990. [[CrossRef](#)]
57. Lei, K.; Ma, F.; Chen, B.; Luo, Y.; Cui, W.; Zhou, Y.; Liu, H.; Sha, T. Three-Dimensional Surface Deformation Characteristics Based on Time Series InSAR and GPS Technologies in Beijing, China. *Remote Sens.* **2021**, *13*, 3964. [[CrossRef](#)]
58. Milillo, P.; Giardina, G.; Perissin, D.; Milillo, G.; Coletta, A.; Terranova, C. Pre-Collapse Space Geodetic Observations of Critical Infrastructure: The Morandi Bridge, Genoa, Italy. *Remote Sens.* **2019**, *11*, 1403. [[CrossRef](#)]
59. Moreira, A.; Prats-Iraola, P.; Younis, M.; Krieger, G.; Hajnsek, I.; Papathanassiou, K.P. A tutorial on synthetic aperture radar. *IEEE Geosci. Remote Sens. Mag.* **2013**, *1*, 6–43. [[CrossRef](#)]
60. Xu, Y.; Gong, H.; Chen, B.; Zhang, Q.; Li, Z. Long-term and seasonal variation in groundwater storage in the North China Plain based on GRACE. *Int. J. Appl. Earth Obs. Geoinf. ITC J.* **2021**, *104*, 102560. [[CrossRef](#)]